Electronic Supplementary Material (ESI) for Journal of Materials Chemistry C.

Supporting Information

Nanoclay-confined single atom catalyst: Tuning uncoordinated N species for efficient water treatment

Xiongbo Dong,[abc] Yinyin Qian,[abc] Zitong Chen,[abc] Zhiyi Jiang,[abc] Aidong Tang[d] and Huaming Yang[abce]*

[a] *Engineering Research Center of Nano-Geomaterials of Ministry of Education, China University of Geosciences, Wuhan 430074, China*

[b] *Faculty of Materials Science and Chemistry, China University of Geosciences, Wuhan 430074, China*

[c] *Key Laboratory of Functional Geomaterials in China Nonmetallic Minerals Industry, China University of Geosciences, Wuhan 430074, China*

[d] *School of Chemistry and Chemical Engineering, Central South University, Changsha 410083, China*

[e] *Hunan Key Laboratory of Mineral Materials and Application, School of Minerals Processing and Bioengineering, Central South University, Changsha 410083, China*

**Corresponding author, Email: hm.yang@cug.edu.cn, hmyang@csu.edu.cn, Fax: +86-27-68788733*

Contents:

Supplementary note 1. Electrochemical measurements

The ITO electrode modified with p-MnNC@Mt-X was first prepared[1]. Nafion solution (5.0 wt% isopropanol in DI water, 0.03 mL), isopropanol (0.50 mL), DI water (0.47 mL), and p-MnNC@Mt-X powder (5 mg) were mixed and dispersed after 60 min ultrasonication. 5 μL of above suspension was dropped onto the surface of ITO electrode, and dried at room temperature under vacuum overnight. Linear sweep voltammogram (LSV) and chronoamperometric curves were performed on an electrochemical workstation (CHI 660E, Shanghai Chenhua Instrument Co., China). The counter, reference, and working electrodes were platinum-wire electrode, saturated calomel electrode, and a modified ITO, respectively. LSV measurements were recorded at the potential scan rate of 5 mV s^{-1} from 0.3 to 1.0 V. Chronoamperometric curves data were obtained at 0.00 V.

Supplementary note 2. EXAFS fitting methods

The obtained XAFS data was processed in Athena (version 0.9.26) for background, pre-edge line and post-edge line calibrations. Then Fourier transformed fitting was carried out in Artemis (version 0.9.26). The k_3 weighting, k-range of 3-12 $Å^{-1}$ and R range of 2-3 Å were used for the fitting of Mn foil. The k-range of 3-6.5 $Å^{-1}$ and R range of 1-3 Å were used for the fitting of Mn. Four parameters, coordination number, bond length, Debye-Waller factor and E_0 shift (CN, R, σ^2, ΔE_0) were fitted without anyone was fixed, constrained, or correlated.

Supplementary note 3. Computational methods

The P-(S, T, or F)-MnC_4, G-(S, T, or F)-MnC_4, P-S-MnN_4, and P-S-MnN_4 surfaces were built, where the vacuum space along the z direction was set to be 20 Å, which was enough to avoid interaction between the two neighboring images. Then, one HSO_5^- was loaded on the surface. All atoms were relaxed adequately. The first principles calculations in the framework of density functional theory were carried out based on the Cambridge Sequential Total Energy Package known as CASTEP.[2] The exchange–correlation functional under the generalized gradient approximation (GGA) with norm-conserving pseudopotentials and Perdew–Burke–Ernzerhof functional was adopted to describe the electron–electron interaction.[3,4] An energy cutoff of 500 eV was used and a k-point sampling set of 6 × 6 × 1

were tested to be converged. A force tolerance of 0.01eV Å $^{-1}$, energy tolerance of 1.0×10^{-5} eV per atom, and maximum displacement of 1.0×10^{-3} Å were considered. The spin unrestricted was used and the Grimme method for DFT-D correction was considered for all calculations[5]. The adsorption energy of A= HSO_5^- was calculated by:[5]

$$\Delta E_A = E_{*A} - E_* - E_A \quad (2)$$

where E_{*A}, E_*, and E_A denote the energy of adsorbed system, clear surface, and A group.

Supplementary note 4. Computational results

As displayed in Fig. 6, we investigated the influence of uncoordinated N species on the interaction between peroxymonosulfate (PMS) and Mn single atom centers via taking uncoordinated N species in second coordination sphere of MnC_4 moieties as a case. The results show that uncoordinated N species around MnC_4 centers affect the release of intermediates via regulating electron localization of Mn, rather than breaking the O–O bonds and the charge transfer between MnC_4 and PMS. Considering that Mn single atoms in p-MnNC@Mt-900 might exist with MnN_4 moieties, the relevant theory calculations were then carried out via taking the MnN_4 moieties surrounded by uncoordinated N species as an example. As displayed in Fig. S27a~27d, the interfacial configurations of two possible models in which MnN_4 centers are surrounded by pyridinic N and graphitic N (denoted as P-S-MnN_4 and G-S-MnN_4), as well as the adsorption structure of PMS molecules on P-S-MnN_4 and G-S-MnN_4, were constructed and optimized. It is found that uncoordinated N species around MnN_4 centers have nearly no effect on breaking the O–O bonds and the charge transfer between MnN_4 and PMS (Fig. S27a-S27d, Table S7).[6-8] In addition, the density of states results suggest that uncoordinated graphitic nitrogen in NG-SACs has a downshifted d-band center of Mn versus pyridinic nitrogen (Fig. S27e). The lower energy level optimizes the bonding energy of the intermediates on single atom centers, accelerating the release of intermediates and regeneration of active sites.[9] In fact, the uncoordinated N species might be not so close to the Mn atoms. Of note, all above similar results could also be obtained although uncoordinated N species are not so close to Mn atoms (Fig. S28&S29). In this regard, it is reasonable to assume that uncoordinated graphitic nitrogen (versus pyridinic nitrogen)

can preferably weaken electronic localization of Mn, thereby accelerating the release of intermediates on Mn single atom centers and enhancing PMS activation efficiency.

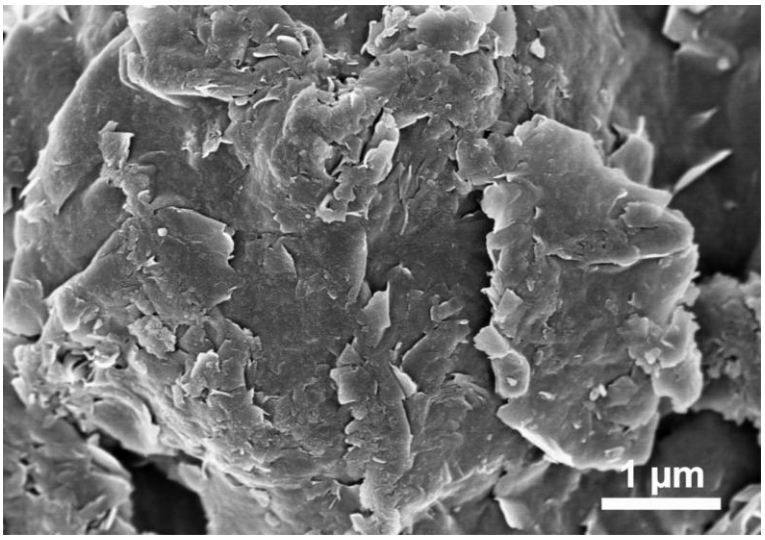

Fig. S1 SEM image of Mt.

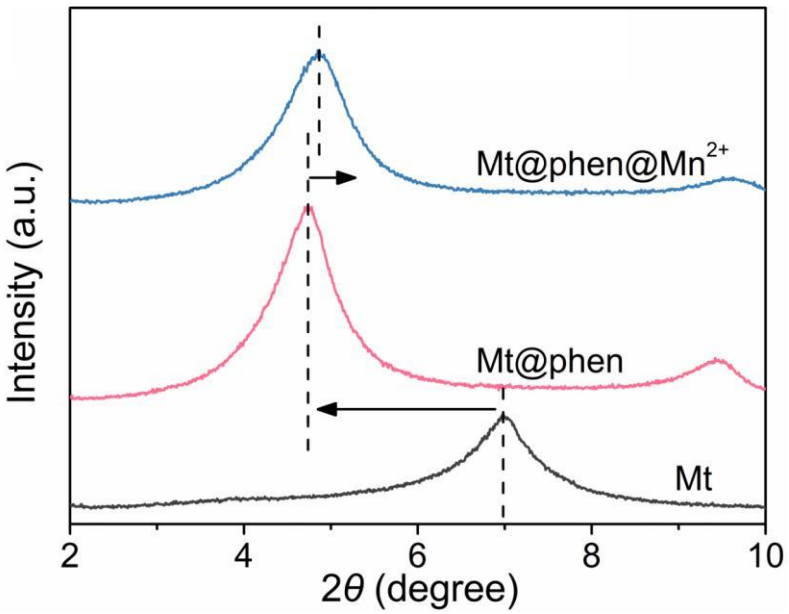

Fig. S2 XRD patterns of Mt, Mt@phen@Mn^{2+}, and MnNC@Mt.

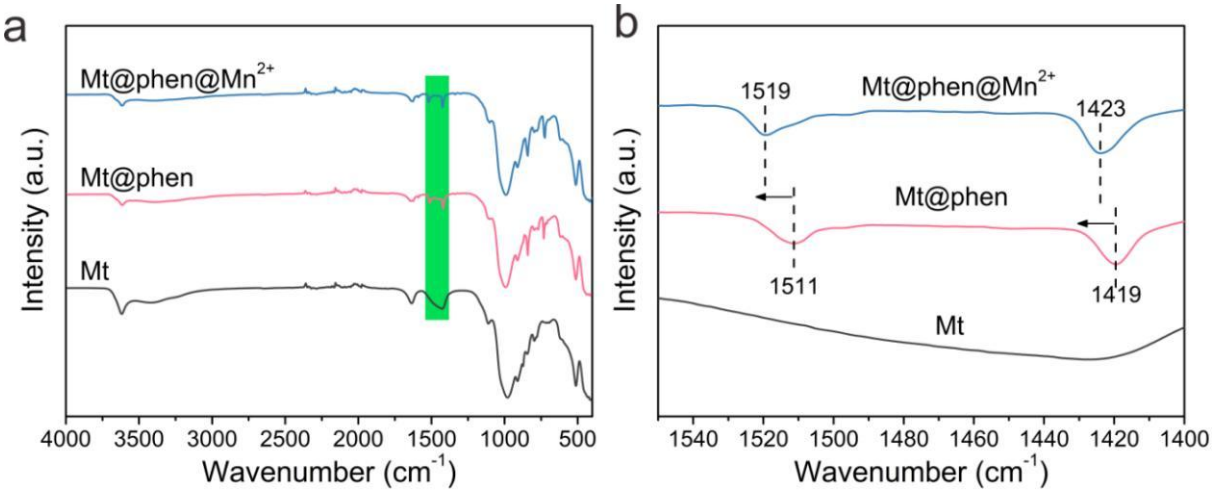

Fig. S3 (a) FTIR spectra of Mt, Mt@phen, and Mt@phen@Mn^{2+}. (b) The corresponding enlarged area marked with green paint in (a).

FTIR was further conducted to clarify the coordination between 1,10-phenanthroline and Mn^{2+}. As shown in Fig. S3, distinct from the FTIR spectra of Mt, two pristine absorption bands located at 1419 and 1511 cm^{-1}, which are assigned to the bending and stretching vibration of C=N in 1,10-phenanthroline respectively, could be detected in that of Mt@phen. This result demonstrates the insertion of 1,10-phenanthroline into the interlayer space of Mt. After the insertion of Mn^{2+} into the interspace of Mt, the blue-shifts observed in above two peaks indicates the coordination between 1,10-phenanthroline and Mn^{2+}, which is consistent with the slight decrease of interlayer spacing of Mt in *ex situ* XRD (Fig. S2).[10]

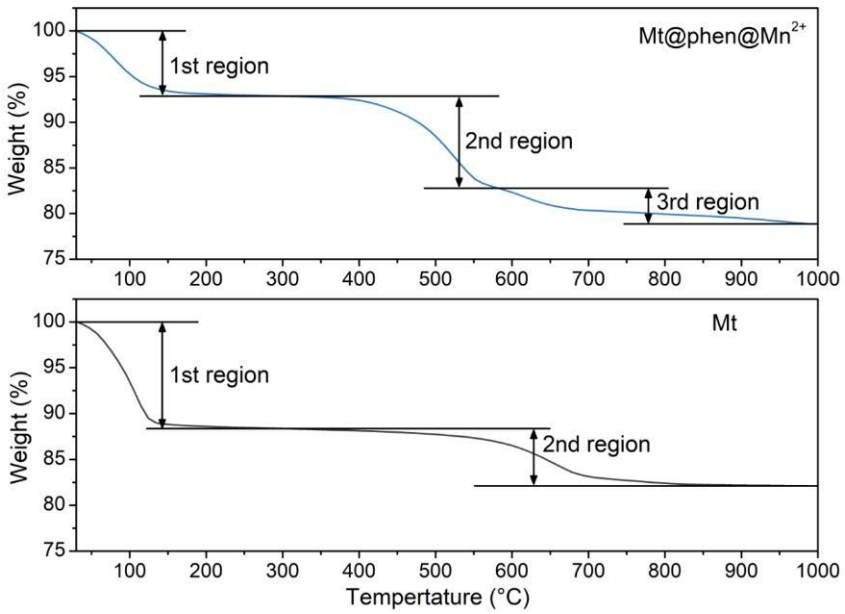

Fig. S4 TGA curve of Mt and Mt@phen@Mn^{2+} under N_2 atmosphere.

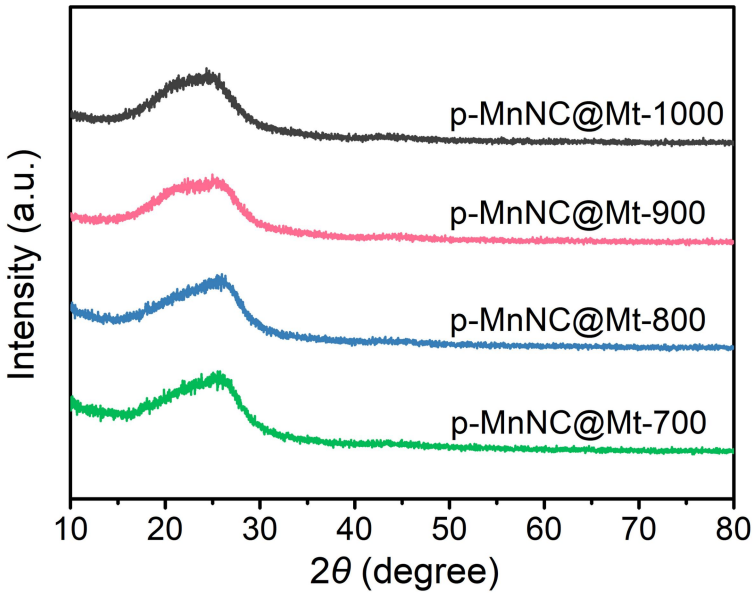

Fig. S5 XRD patterns for p-MnNC@Mt-X (X = 700, 800, 900, and 1000).

No Mn metal peak observed in p-MnNC@Mt-X demonstrates the possible formation of single Mn atoms (Fig. S5).

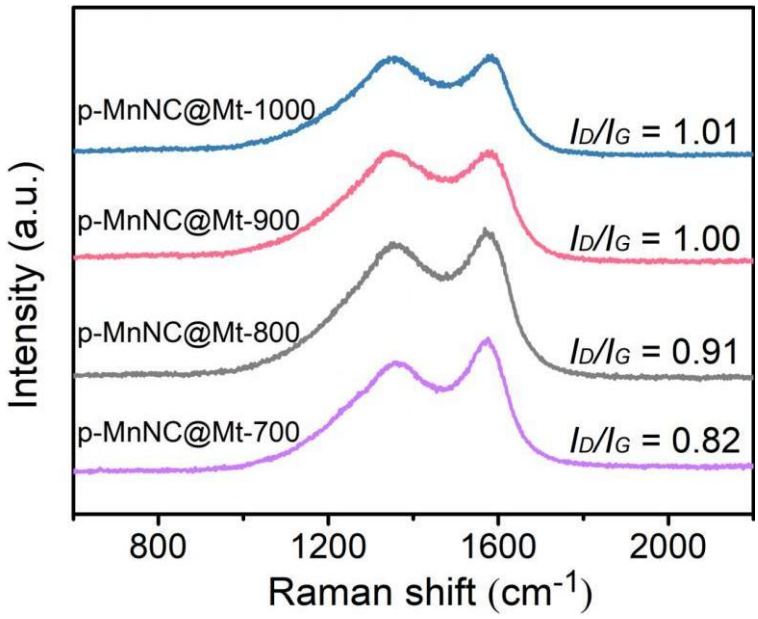

Fig. S6 Raman spectroscopy of p-MnNC@Mt-X.

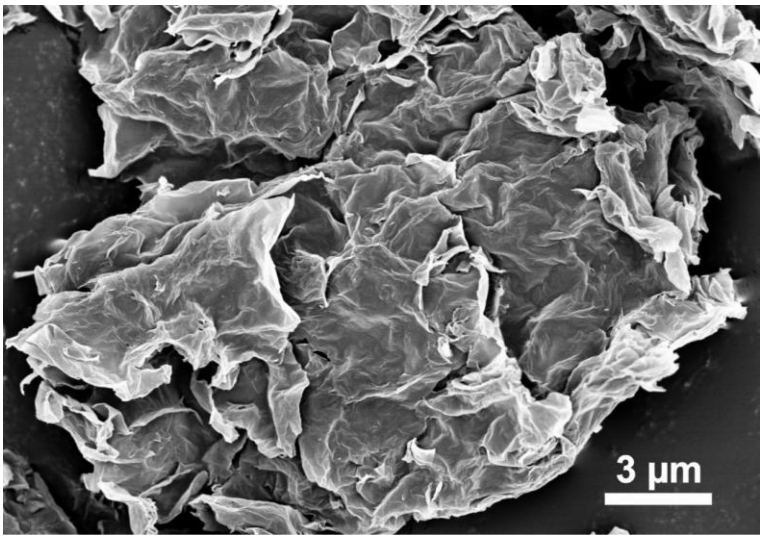

Fig. S7 SEM image of p-MnNC@Mt-900.

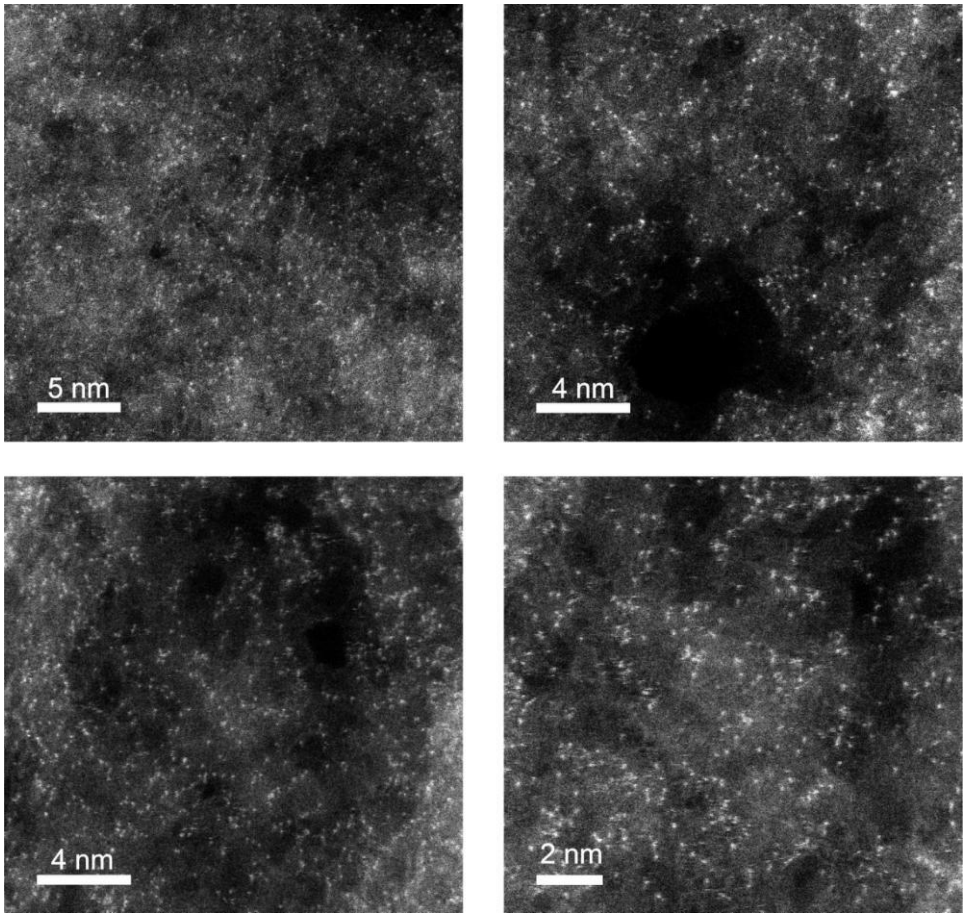

Fig. S8 HADDF-STEM images of p-MnNC@Mt-900.

To provide convincing proofs for the generation of Mn single atoms, more HADDF-STEM images of p-MnNC@Mt-900 were recorded. As seen in Fig. S8, no nanoparticles or clusters are detected in all the HADDF-STEM images. In addition, the clearly exclusive bright dots in HADDF-STEM images further identify the existence of isolated Mn single atoms in p-MnNC@Mt-900.

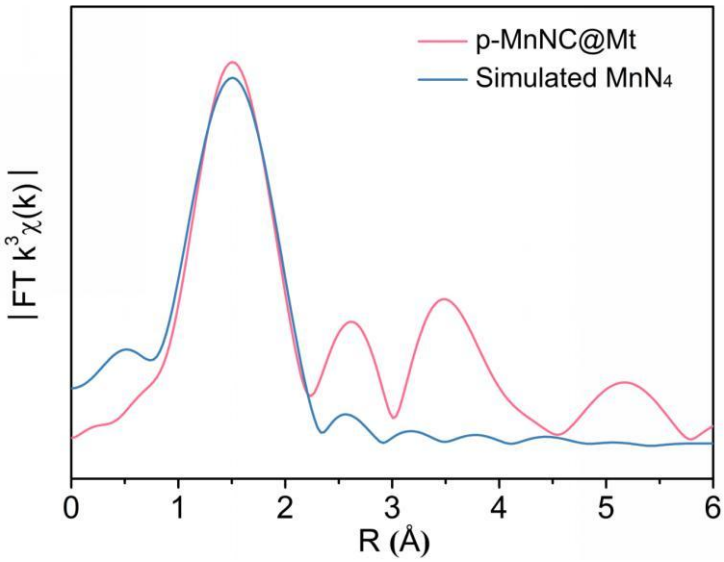

Fig. S9 The prediction of Fourier-transformed k^3-weighted EXAFS curve (R space) for MnN_4.

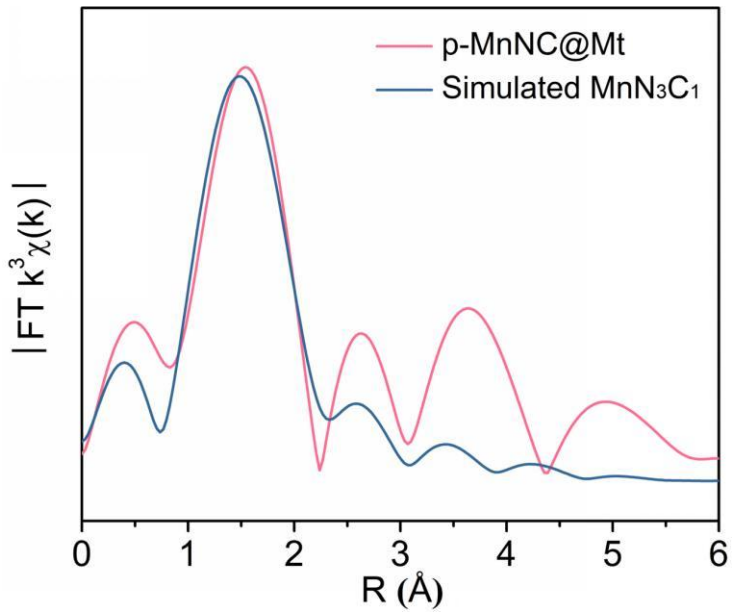

Fig. S10 The prediction of Fourier-transformed k^3-weighted EXAFS curve (R space) for MnN_3C_1.

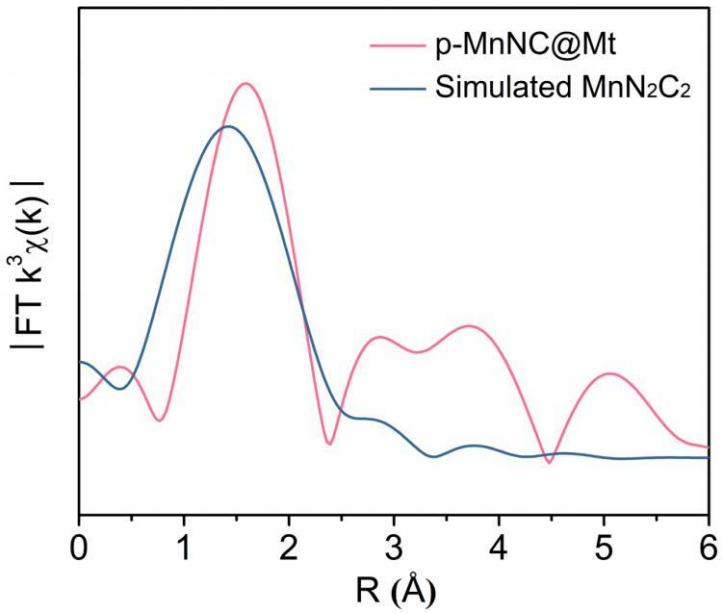

Fig. S11 The prediction of Fourier-transformed k^3-weighted EXAFS curve (R space) for MnN_2C_2.

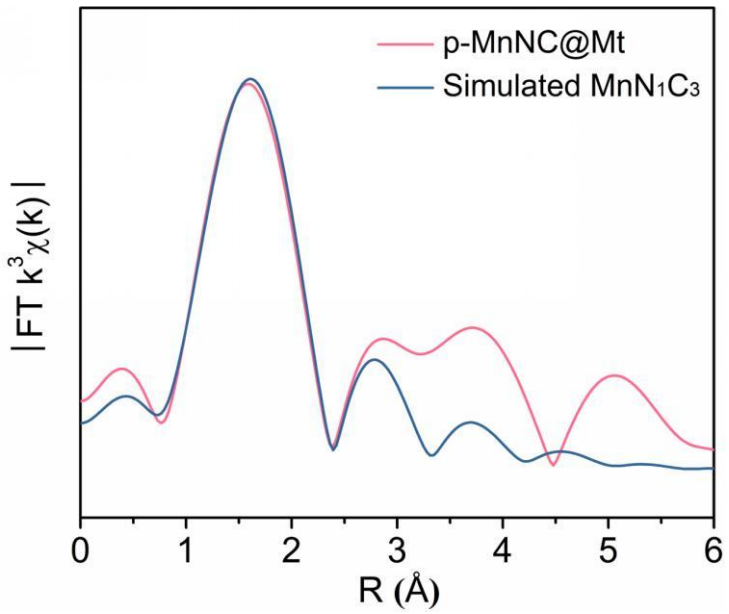

Fig. S12 The prediction of Fourier-transformed k^3-weighted EXAFS curve (R space) for MnN_1C_3.

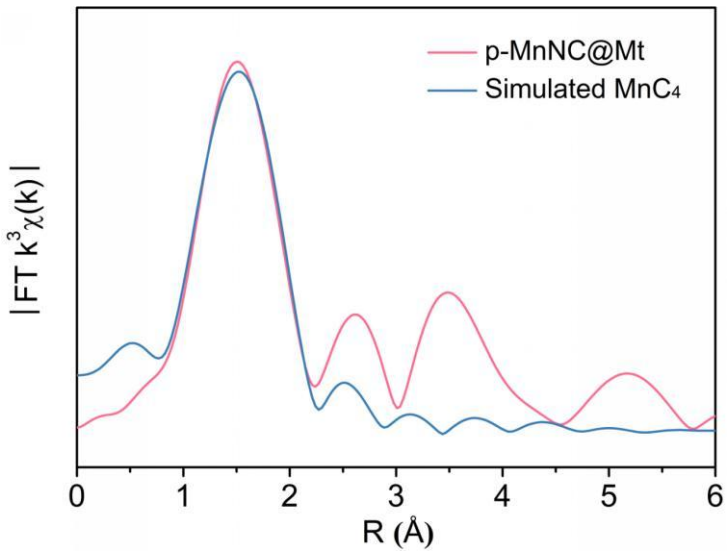

Fig. S13 The prediction of Fourier-transformed k^3-weighted EXAFS curve (R space) for MnC_4.

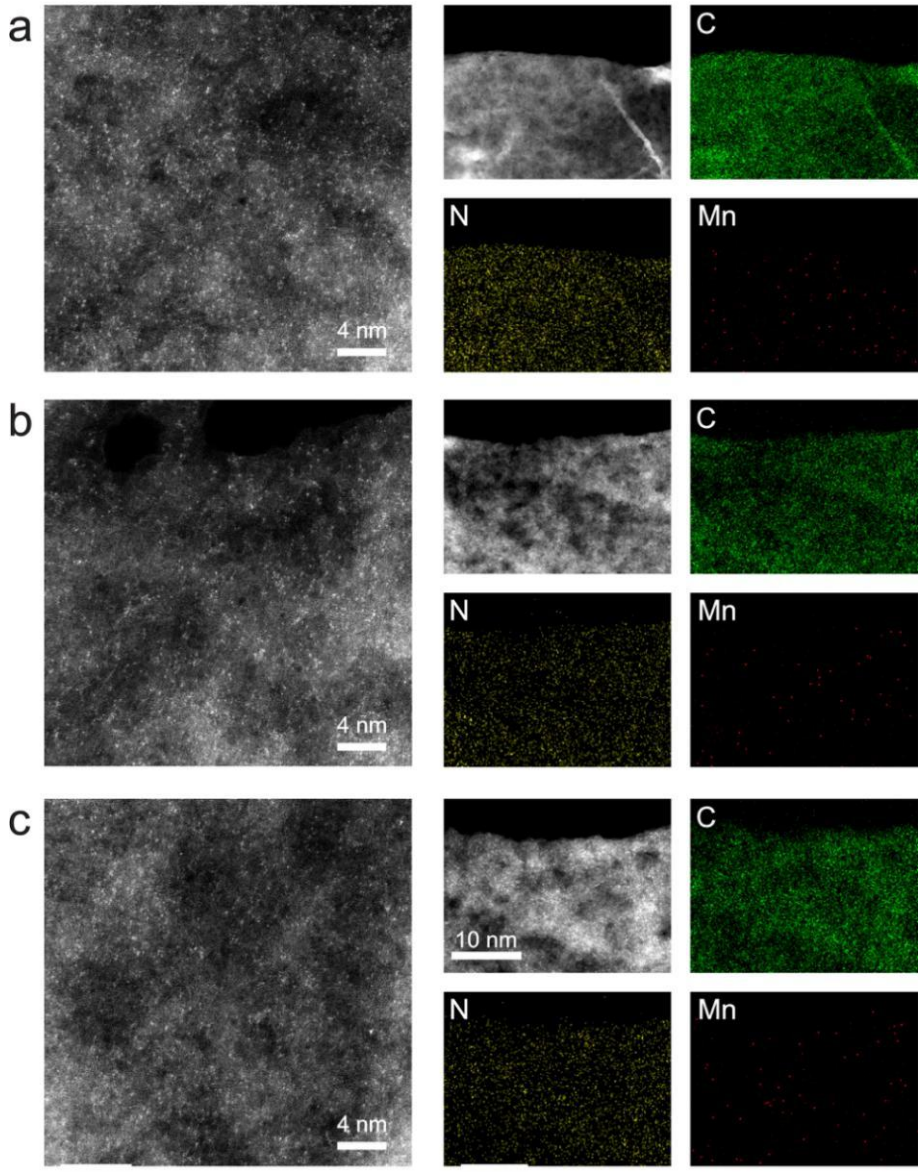

Fig. S14 HADDF-STEM images and corresponding EDX mappings of (a) p-MnNC@Mt-700, (b) p-MnNC@Mt-800 and (c) p-MnNC@Mt-1000.

The exclusive bright dots and the homogeneous distribution of Mn, N and C atoms could be detected in HADDF-STEM images and corresponding energy dispersive X-ray (EDX) mappings of all p-MnNC@Mt-X samples despite changing the pyrolysis temperature (Fig. S14). These results demonstrate that our proposed nano-confinement strategy is a general method for NG-SACs.

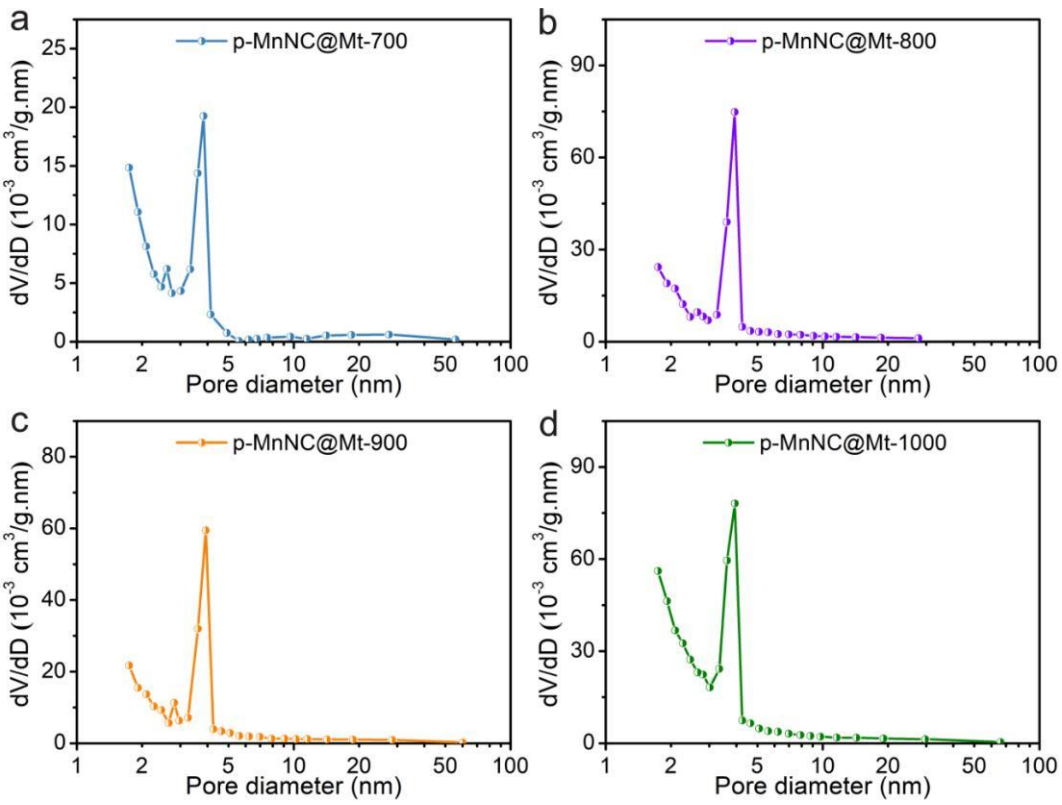

Fig. S15 Pore size distributions for p-MnNC@Mt-X (X = 700, 800, 900, and 1000).

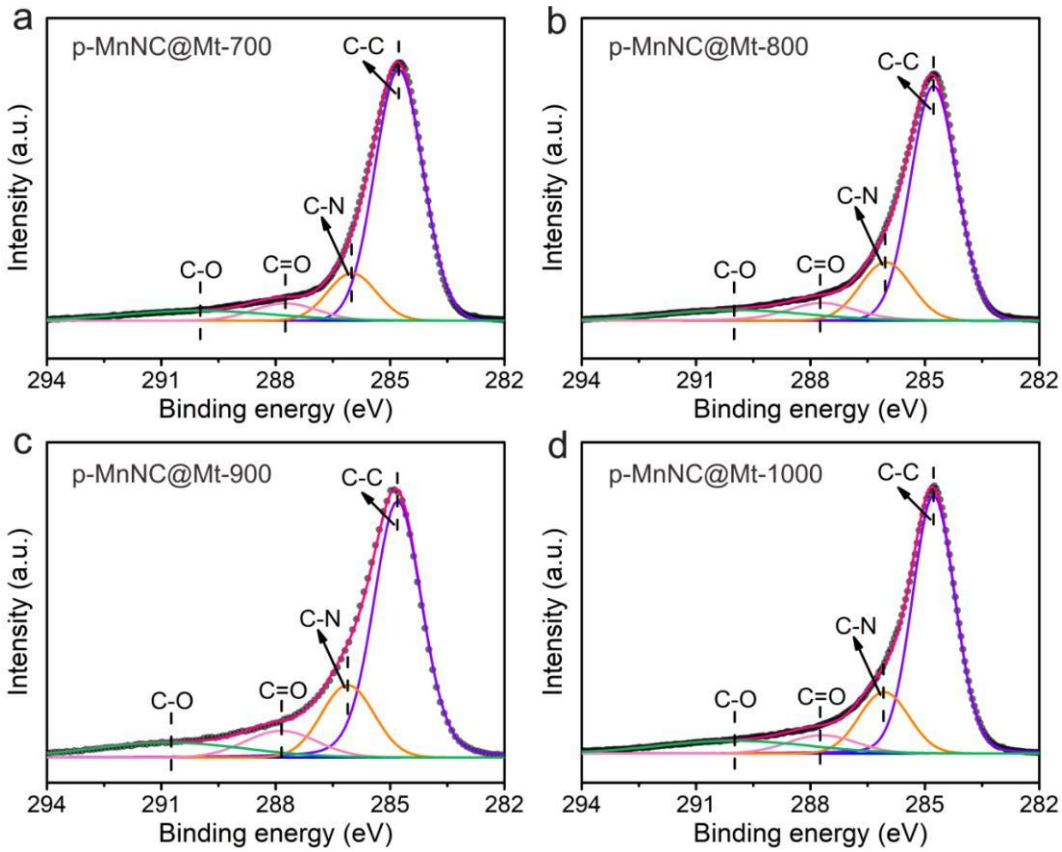

Fig. S16 Deconvolution of the high-resolution of C1s for p-MnNC@Mt-X (X = 700, 800, 900, and 1000).

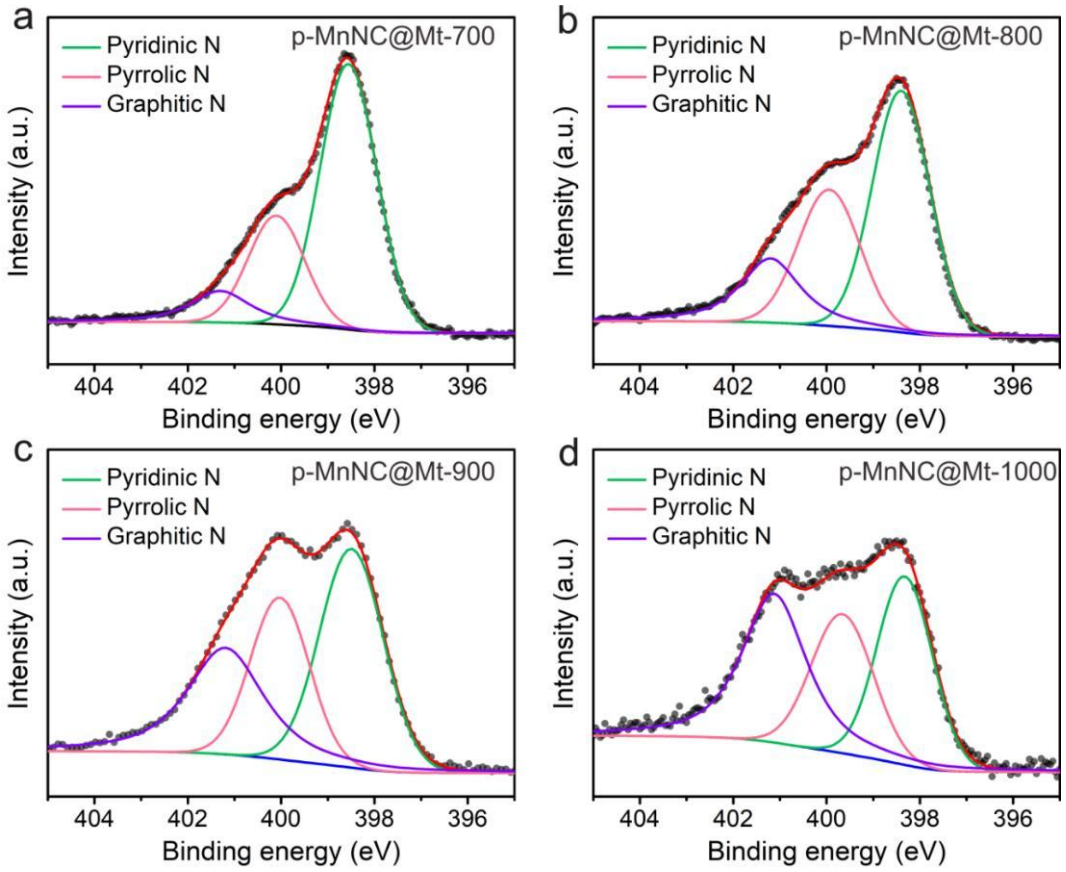

Fig. S17 Deconvolution of the high-resolution of N1s for p-MnNC@Mt-X (X = 700, 800, 900, and 1000).

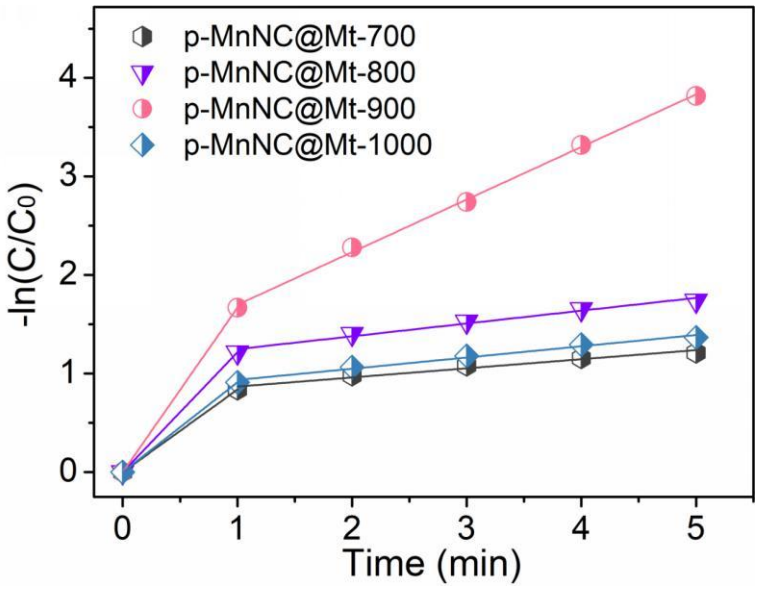

Fig. S18 Pseudo-first-order kinetics for BPA degradation in p-MnNC@Mt-X/PMS systems. Experimental conditions: $[BPA]_0$ = 10 mg/L; $[Catalyst]_0$ = 0.1 g/L; $[PMS]_0$ = 1.0 mM.

As displayed in Fig. S18, a two-stage oxidation process could be observed in all p-MnNC@Mt-X/PMS systems. Previous study has proven that the initial stage was ascribed to the direct electron transfer between catalysts, PMS and organic molecules.[11] In this work, the direct electron transfer process dominates the BPA degradation in all p-MnNC@Mt-X/PMS systems. In this regard, the initial stage was used to determine the BPA removal rate constant (k).

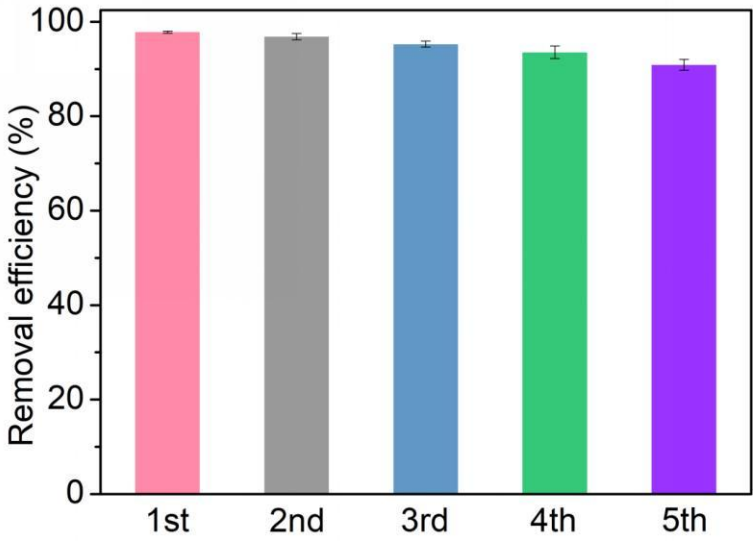

Fig. S19 BPA degradation efficiency in five consecutive runs by p-MnNC@Mt-900/PMS system. Experimental conditions: $[BPA]_0$ = 10 mg/L; $[Catalyst]_0$ = 0.1 g/L; $[PMS]_0$ = 0.6 mM.

After five consecutive runs, p-MnNC@Mt-900 still shows the excellent PMS activation efficiency for BPA removal (Fig. S19).

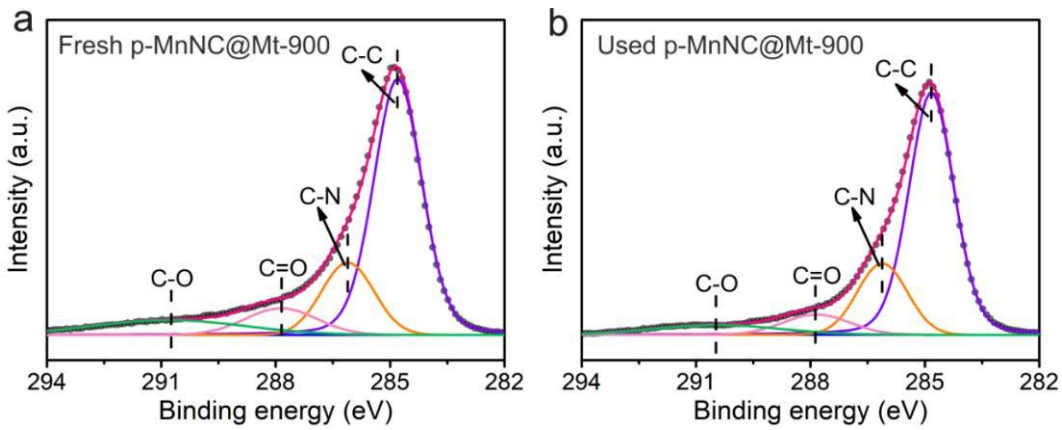

Fig. S20 C 1s photoemission spectra of fresh and used p-MnNC@Mt-900.

The C 1s core-level spectra of fresh and used p-MnNC@Mt-900 could be well divided into four peaks, which is ascribed to C-O, C=O, C-N, and C-C (Fig. S20). These carbon-based functional groups of p-MnNC@Mt-900 show negligible changes after 5 cycle runs.

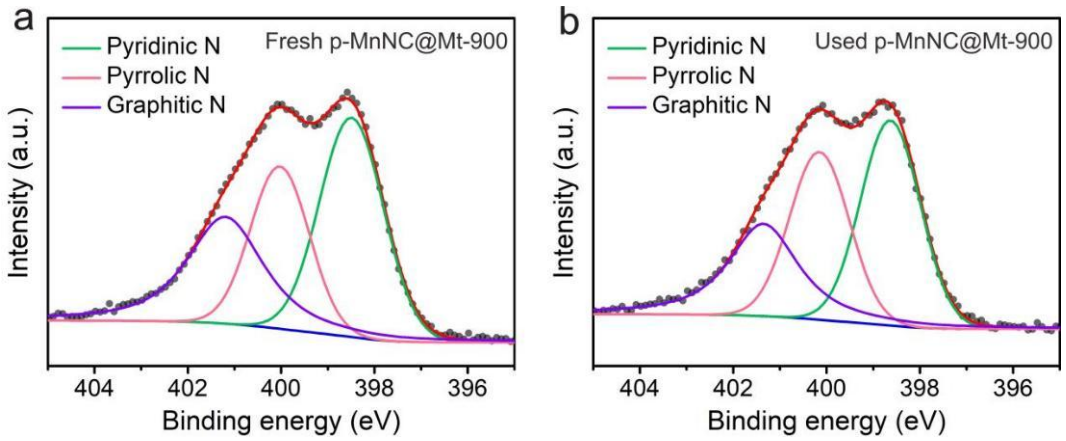

Fig. S21 N 1s photoemission spectra of fresh and used p-MnNC@Mt-900.

The p-MnNC@Mt-900 preserves the ratio of pyridinic N, pyrrolic N, and graphitic N (Fig. S21).

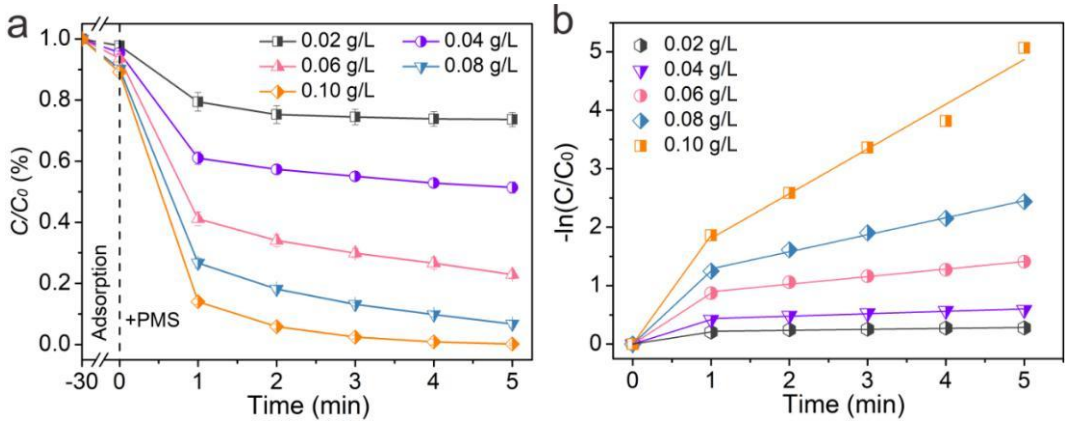

Fig. S22 (a) Effect of catalyst dosage on BPA degradation catalyzed by p-MnNC@Mt-900/PMS system. (b) The corresponding pseudo-first-order kinetics. Experimental conditions: $[BPA]_0$ = 10 mg/L; $[PMS]_0$ = 1.0 mM.

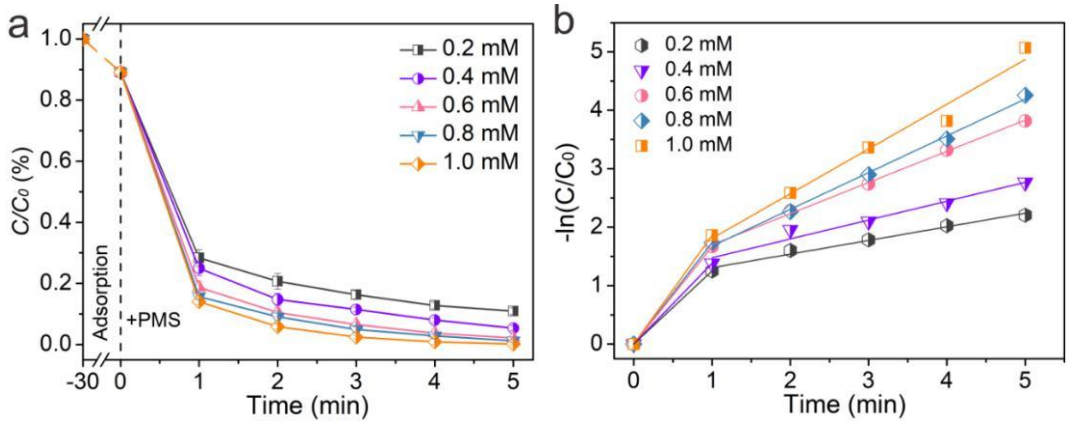

Fig. S23 (a) Effect of PMS concentration on BPA degradation catalyzed by p-MnNC@Mt-900/PMS system. (b) The corresponding pseudo-first-order kinetics. Experimental conditions: $[BPA]_0$ = 10 mg/L; $[Catalyst]_0$ = 0.1 g/L.

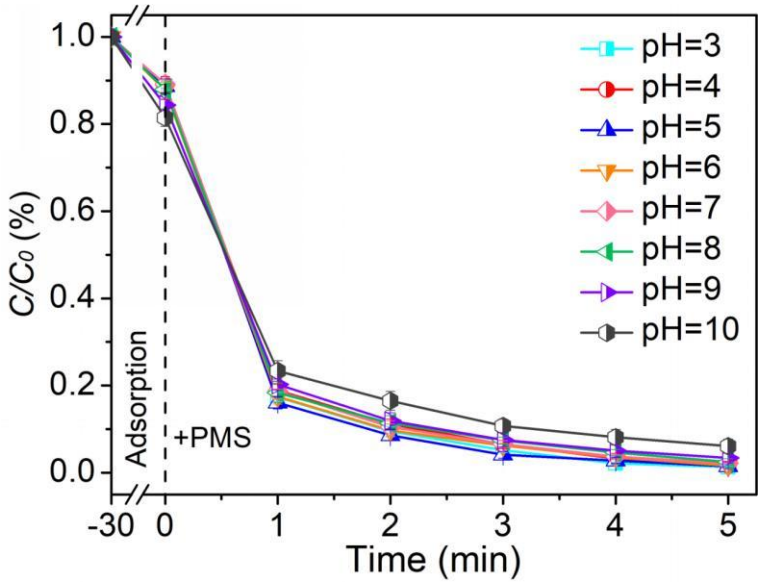

Fig. S24 Effect of initial pH value on BPA degradation catalyzed by p-MnNC@Mt-900/PMS system. Experimental conditions: $[BPA]_0$ = 10 mg/L; $[Catalyst]_0$ = 0.1 g/L; $[PMS]_0$ = 0.6 mM.

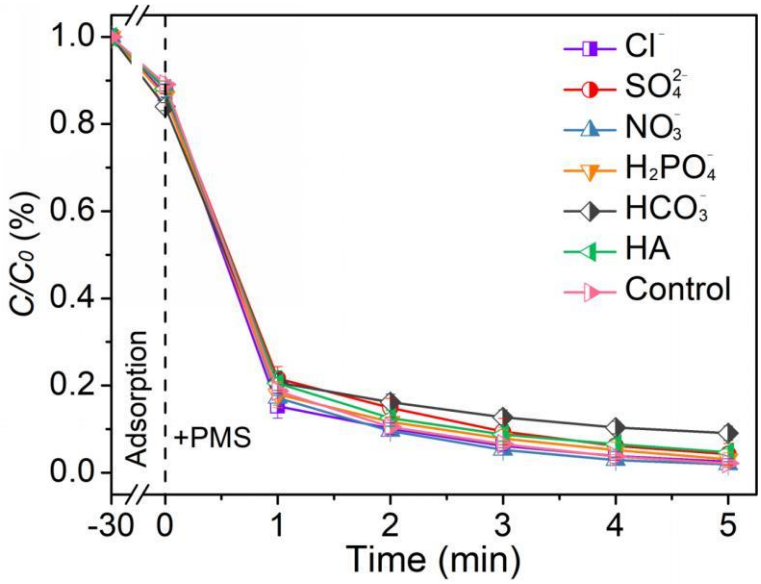

Fig. S25 Effects of inorganic anions and HA ($[NO_3^-]$ = $[SO_4^{2-}]$ = $[Cl^-]$ = $[H_2PO_4^-]$ = $[HCO_3^-]$ = 20 mM; [HA] = 20 mg/L) on BPA degradation catalyzed by p-MnNC@Mt-900/PMS system. Experimental conditions: $[BPA]_0$ = 10 mg/L; $[Catalyst]_0$ =0.1 g/L; $[PMS]_0$ = 0.6 mM.

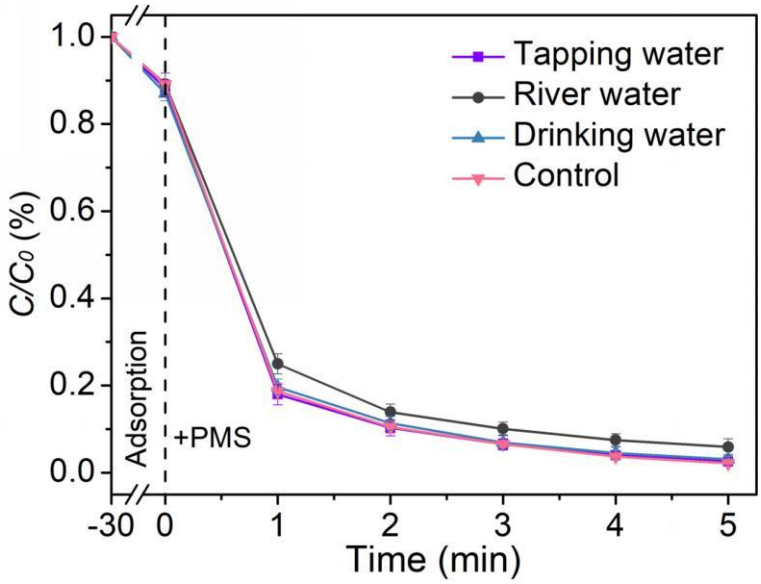

Fig. S26 BPA degradation efficiency in different water matrix by p-MnNC@Mt-900/PMS system. Experimental conditions: $[BPA]_0$ = 10 mg/L; $[Catalyst]_0$ = 0.1 g/L; $[PMS]_0$ = 0.6 mM.

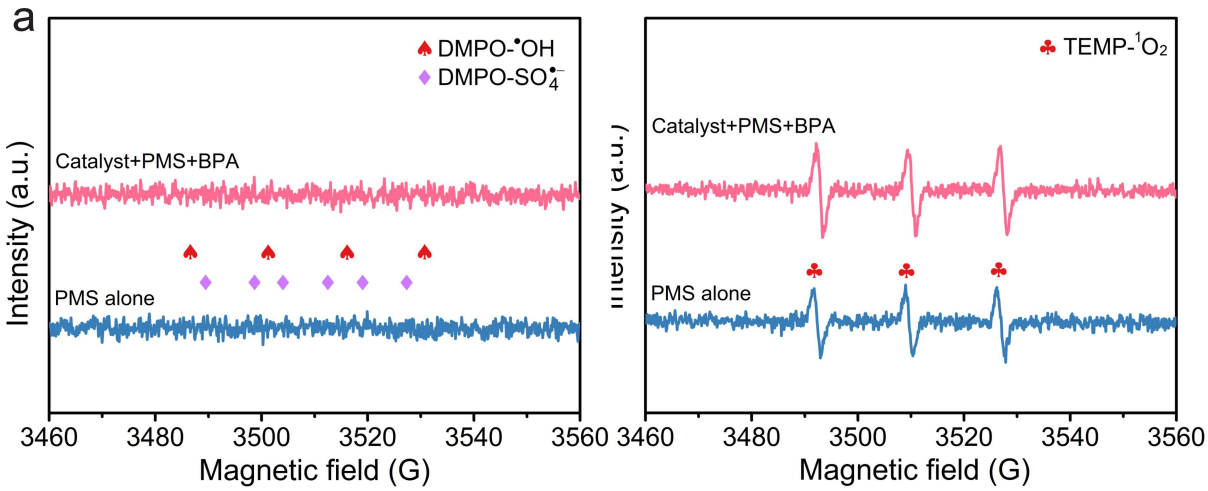

Fig. S27 EPR spectra obtained in p-MnNC@Mt-900/PMS/BPA system using (a) DMPO and (b) TEMP as spin-trapping agents.

The EPR characterization has been added to further verify the reaction mechanisms. As seen in Fig. S27a, no detectable characteristic signals ascribed to DMPO–$SO_4^{\bullet-}$ or DMPO–$^{\bullet}$OH adducts demonstrates absence of radical pathway ($SO_4^{\bullet-}$ or $^{\bullet}$OH) in p-MnNC@Mt-900/PMS/BPA system. A set of characteristic signals for TEMP–$^1O_2$ adducts were observed in both PMS/TEMP and p-MnNC@Mt-900/PMS/BPA/TEMP systems with the similar peak intensity (Fig. S27b). This phenomenon could be attributed to the self-decomposition of PMS, further excluding the nonradical pathway during PMS activation. Above results are well consistent with the scavenging experiments (Fig. 5b). Furthermore, the direct electron transfer pathway was evidenced by *in situ* Raman, chronoamperometric, and LSV analyses (Fig. 5c~5e).

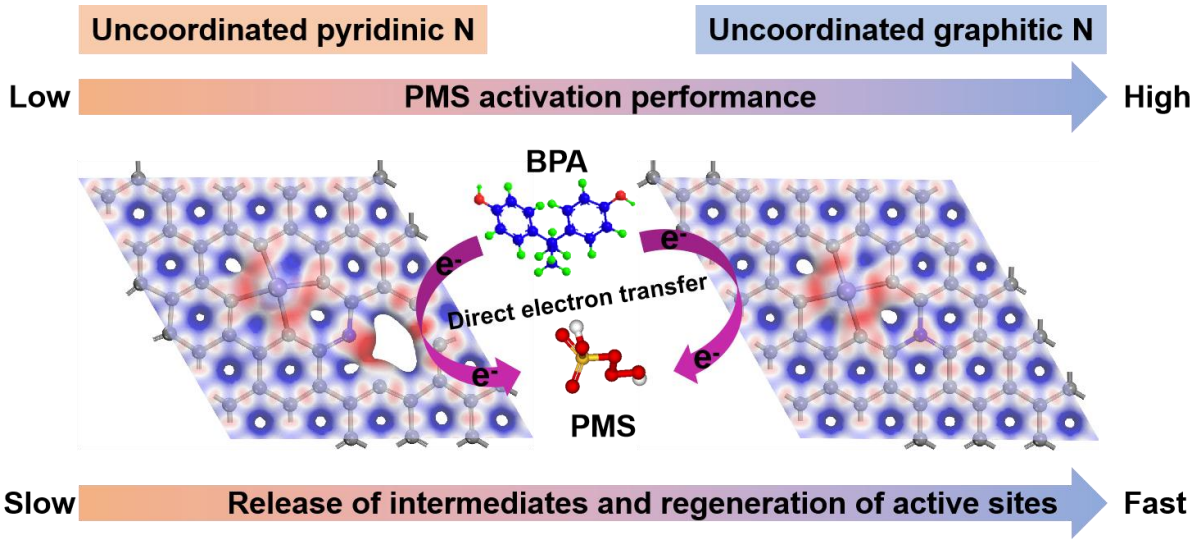

Fig. S28 Schematic outline for the mechanism of p-MnNC@Mt-X in PMS activation.

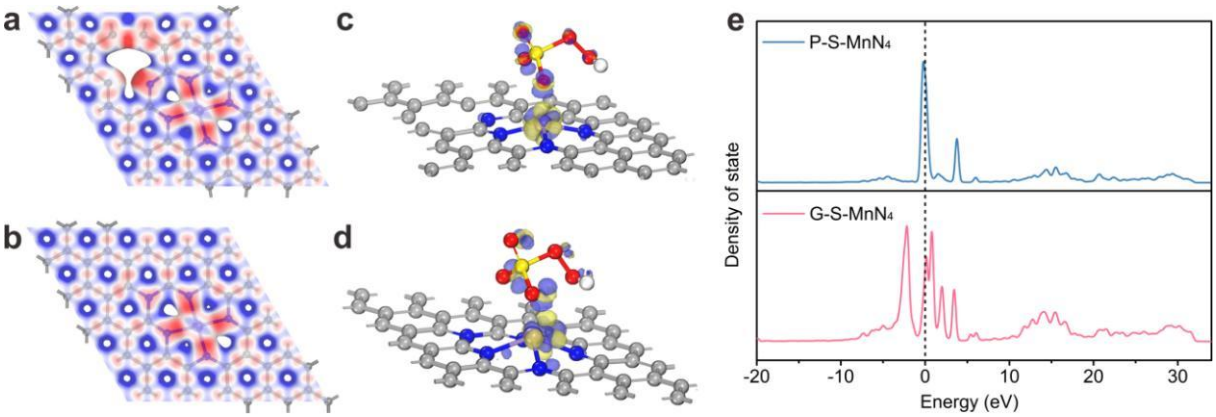

Fig. S29 3D differential charge densities of MnN_4 centers surrounded by (a) pyridinic N (denoted as P-S-MnC_4) and (b) graphitic N (denoted as G-S-MnN_4) occupied in second coordination sphere. 3D differential charge densities of PMS molecules adsorbed on MnN_4 centers of (c) P-S-MnN_4 and (d) G-S-MnN_4. The projected density of states of Mn 3d in (e) P-S-MnN_4 and G-S-MnN_4. The isovalue of electron density is set to 0.07 e/Å^3.

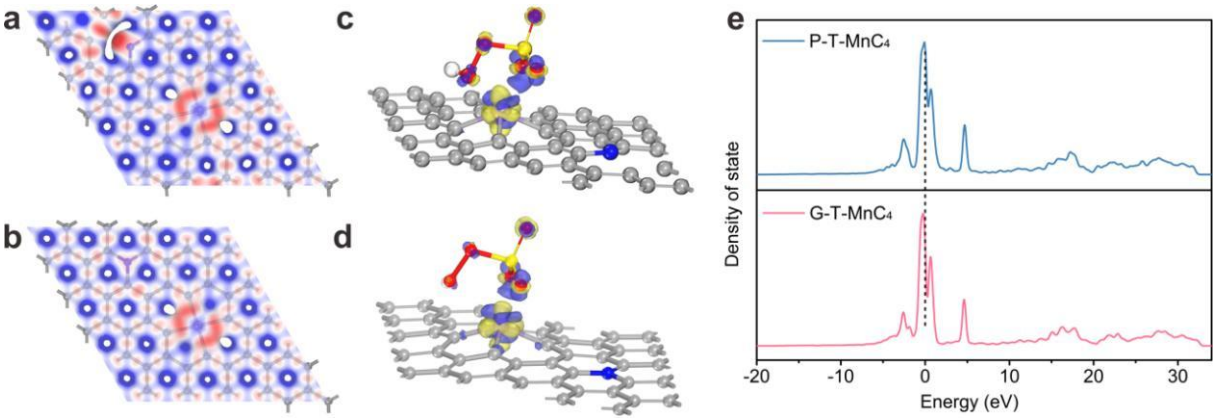

Fig. S30 3D differential charge densities of (a) P-T-MnC_4 and (b) G-T-MnC_4. 3D differential charge densities of PMS molecules adsorbed on MnC_4 centers of (c) P-T-MnC_4 and (d) G-T-MnC_4. The projected density of states of Mn 3d in (e) P-T-MnC_4 and G-T-MnC_4. The isovalue of electron density is set to 0.07 e/$Å^3$.

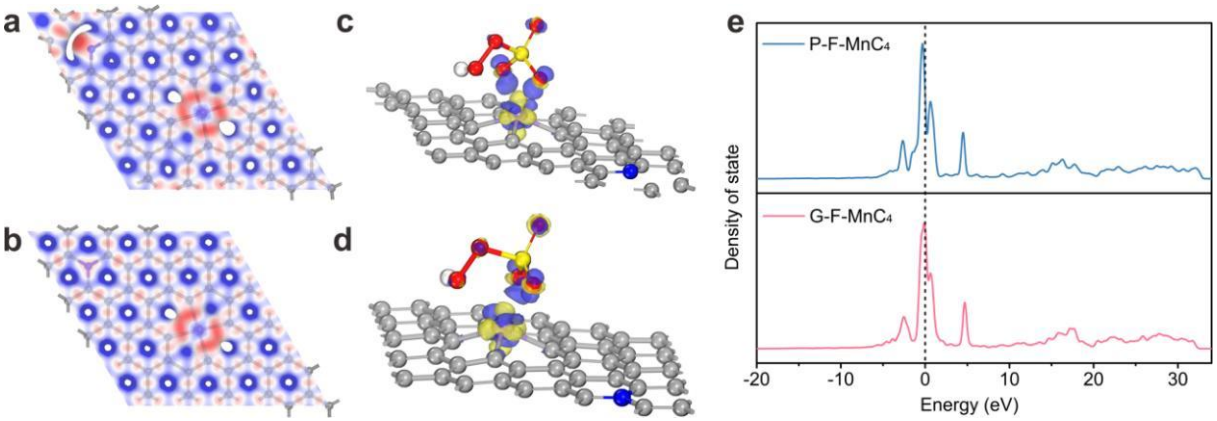

Fig. S31 3D differential charge densities of MnC_4 centers surrounded by (a) pyridinic N (denoted as P-F-MnC_4) and (b) graphitic N (denoted as G-F-MnC_4) occupied in forth coordination sphere. 3D differential charge densities of PMS molecules adsorbed on MnC_4 centers of (c) P-F-MnC_4 and (d) G-F-MnC_4. The projected density of states of Mn in (e) P-F-MnC_4 and G-F-MnC_4. The isovalue of electron density is set to 0.07 e/Å^3.

Table S1 The chemical composition of Mt (wt %).

SiO_2	Al_2O_3	CaO	Fe_2O_3	Na_2O	MgO	K_2O	TiO_2
62.63	17.72	5.04	4.76	4.15	3.87	1.02	0.25

Table S2 The chemical composition of p-MnNC@Mt-900 (at %).

C	N	O	Mn	Si	Al
83.16	9.51	6.54	0.02	0.27	0.50

Table S3 The interlayer spacing of intermediates during the synthesis of p-MnNC@Mt-900. Herein, the basal plane spacing of Mt, which is equal to the sum of interlayer spacing and thickness of one Mt layer, was calculated by Bragg equation. The thickness of one Mt layer is 0.96 nm.

Samples	Interlayer spacing (d, nm)
Mt	0.32
Mt@phen	0.91
Mt@phen@Mn^{2+}	0.86
MnNC@Mt-900	0.36
Mt-900	—

Table S4 Structural parameters extracted from the Mn K-edge EXAFS fitting.

Samples	Scattering pair	CN	R (Å)	$\sigma^2\times10^3$ (Å^2)	R factor
Mn foil	Mn-Mn	12	2.66	5.6	0.012
p-MnNC@Mt-900	Mn-C/N	4.2	1.93	4.8	0.017
MnN_4	Mn-C	4	2.03	15.4	0.009
MnC_1N_3	Mn-C	1	1.94	5.6	0.050
	Mn-N	3	1.83		
MnC_2N_2	Mn-C	2	1.97	16.2	0.118
	Mn-N	2	1.54		
MnC_3N_1	Mn-C	3	1.85	-12.6	0.010
	Mn-N	1	1.57		
MnC_4	Mn-N	4	2.05	11.2	0.006

CN is the coordination number; R is interatomic distance (the bond length between Mn central atoms and surrounding coordination atoms); σ^2 is Debye-Waller factor (a measure of thermal and static disorder in absorber-scatterer distances); R factor is used to value the goodness of the fitting.

Table S5 Mn loadings of p-MnNC@Mt-X determined by inductively coupled plasma mass spectroscopy.

Samples	Mn (wt%)
p-MnNC@Mt-700	0.11
p-MnNC@Mt-800	0.11
p-MnNC@Mt-900	0.10
p-MnNC@Mt-1000	0.05

Table S6 Surface and structure characterization of p-MnNC-900, Mt, and p-MnNC@Mt-X.

Samples	BET surface area (m^2/g)
p-MnNC@Mt-700	120.1
p-MnNC@Mt-800	262.1
p-MnNC@Mt-900	280.4
p-MnNC@Mt-1000	428.6

Table S7 Relative amount of N species in p-MnNC-900 and p-MnNC@Mt-X.

Samples	Graphitic N	Pyrrolic N	Pyridinic N	N content (at%)
p-MnNC@Mt-700	10.90	25.80	63.29	10.91
p-MnNC@Mt-800	19.13	30.43	50.43	11.46
p-MnNC@Mt-900	31.55	27.70	40.76	9.51
p-MnNC@Mt-1000	40.15	27.04	32.81	7.93

Table S8 The Mn loadings of fresh and used p-MnNC@Mt-900 determined by inductively coupled plasma mass spectroscopy.

Samples	Mn (wt%)
Fresh p-MnNC@Mt-900	0.10
Used p-MnNC@Mt-900	0.10

Table S9 The relevant calculation results of PMS adsorption on P-(S, T, F)-MnC_4, G-(S, T, F)-MnC_4, P-S-MnN_4, G-S-MnN_4, PMS-P-(S, T, F)-MnC_4, PMS-G-(S, T, F)-MnC_4, PMS-P-S-MnN_4, and PMS-G-S-MnN_4 surfaces. The adsorption energy E_{ads} and bond length $l_{O–O}$ between –OH group and $–SO_4$ group are listed.

Models	E_{ads} (eV)	lo–o (Å)
PMS	—	1.373
PMS-P-S-MnC_4	-3.11	1.491
PMS-G-S-MnC_4	-2.88	1.494
PMS-P-T-MnC_4	-2.97	1.473
PMS-G-T-MnC_4	-2.86	1.473
PMS-P-F-MnC_4	-2.94	1.473
PMS-G-F-MnC_4	-2.85	1.477
PMS-P-S-MnN_4	-3.82	1.480
PMS-G-S-MnN_4	-3.12	1.481

Table S10 The Mn leaching of p-MnNC@Mt-900 determined by inductively coupled plasma mass spectroscopy.

Samples	Mn (wt%)
Mn leaching	~

References

1 X. Dong, Z. Chen, A. Tang, D. D. Dionysiou and H. Yang, *Adv. Funct. Mater.*, 2022, 2111565.

2 M. D. Segall, P. J. D. Lindan, M. J. Probert, C. J. Pickard, P. J. Hasnip, S. J. Clark*, M. C. Payne, J. Phys.Condens. Mat.* **2002**, 14, 2717.

3 J. P. Perdew, K. Burke, M. Ernzerhof, *Phys. Rev. Lett.* **1996**, 77, 3865.

4 S. Grimme, *J. Comput. Chem.* **2006**, 27, 1787.

5 D. R. Hamann, M. Schlüter, C. Chiang, *Phys. Rev. Lett.* **1979**, 43, 1494.

6 X. Duan, Z. Ao, H. Sun, L. Zhou, G. Wang and S. Wang, *Chem. Commun.*, 2015, **51**, 15249-15252.

7 C. Chu, J. Yang, X. Zhou, D. Huang, H. Qi, S. Weon, J. Li, M. Elimelech, A. Wang and J. Kim*, Environ. Sci. Technol.,* 2021, **55**, 1242.

8 J. Miao, Y. Zhu, J. Lang, J. Zhang, S. Cheng, B. Zhou, L. Zhang, P. J. J. Alvarez and M. Long, *Environ. Sci. Technol., 2021, **11**, 9569-9577.*

9 S. Zuo, D. Li, Z. Guan, F. Yang, H. Xu, D. Xia and J. Wan, *ACS Appl. Mater. Inter.*, 2021, **13**, 49982-49992.

10 K. K. Bania, R. C. Deka, *J. Phys. Chem. C*, 2012, **116**, 14295−14310.

11 W. Ren, G. Nie, P. Zhou, H. Zhang, X. Duan and S. Wang, *Environ. Sci. Technol.*, 2020, **54**, 6438−6447.